REPORT

Cell cycle– and genomic distance–dependent dynamics of a discrete chromosomal region

Hanhui Ma[1]*, Li-Chun Tu[2]*, Yu-Chieh Chung[4]*, Ardalan Naseri[3], David Grunwald[2], Shaojie Zhang[3], and Thoru Pederson[1]

In contrast to the well-studied condensation and folding of chromosomes during mitosis, their dynamics during interphase are less understood. We deployed a CRISPR-based DNA imaging system to track the dynamics of genomic loci situated kilobases to megabases apart on a single chromosome. Two distinct modes of dynamics were resolved: local movements as well as ones that might reflect translational movements of the entire domain within the nucleoplasmic space. The magnitude of both of these modes of movements increased from early to late G1, whereas the translational movements were reduced in early S phase. The local fluctuations decreased slightly in early S and more markedly in mid-late S. These newly observed movements and their cell cycle dependence suggest the existence of a hitherto unrecognized compaction–relaxation dynamic of the interphase chromosome fiber, operating concurrently with changes in the extent of overall movements of loci in the 4D genome.

Introduction

The chromosomes as seen in mitosis (Flemming, 1882) riveted attention to this dramatic performance and naturally diverted thoughts on the status of the chromosomes during interphase. This remained so for a century until two cell biologists working at the temporal junction of the premodern and modern eras of the nucleus field, Daniel Mazia and David Prescott, independently speculated that there is a continuous cycle of chromosome decondensation–recondensation occurring throughout interphase, but below the level of cytological detection. Evidence in support of this idea soon came (Pederson, 1972; Pederson and Robbins, 1972). Then, in 1996, a breakthrough occurred with the development of a lac operator/repressor-based system that allowed eukaryotic chromosomal sites to be visualized (Robinett et al., 1996).

This methodological revolution led to subsequent iterations and key studies in which the movements of the tagged chromosomal sites were tracked (Heun et al.,2001), and this field has recently advanced even further (Chen et al., 2013; Gu et al., 2018). Our longstanding interest in interphase chromosome dynamics became reactivated in the context a series of CRISPR-based chromosome labeling platforms we have developed (Ma et al., 2015, 2016a,b). In the present study, we tracked not a single chromosomal locus, as in the earlier pioneer studies, but rather examined pairs of loci situated in a particular chromosomal region, with these pairs having shorter versus longer inter-locus distances along the chromosome. In this way we have defined, for the first time, the dynamics of an interphase chromosome within these boundary lines, as a local parameter that is a defined segment of the chromosome.

Proper spatial organization and dynamics of chromosomes at the kilobase to megabase scales are essential for gene regulation and cellular function (Risca and Greenleaf, 2015). DNA FISH and super-resolution microscopy in fixed cells allow measurement of the distances between loci at tens of nanometers resolution (Boettiger et al., 2016), while chromosome conformation capture identifies DNA loops as well as apparently autonomous genomic domains and compartments at kilobase resolution by measuring contact probabilities between pairs of loci in a cell population (Lieberman-Aiden et al., 2009; Rao et al., 2014). These methods have revealed a number of chromosome structure features in a static mode, including folding, compaction, and organization in different cellular conditions. Chromatin compaction has been found to be regulated at all scales investigated so far, from the entire chromosome such as the X (Teller et al., 2011) or large intra-chromosomal domains such as the polycomb gene locus (Francis et al., 2004; Boettiger et al., 2016), to the level of single genes (Jubb et al., 2017). An inherent limitation of chromosome capture studies, namely, that they had been limited to ensemble

[1]Department of Biochemistry and Molecular Pharmacology, University of Massachusetts Medical School, Worcester, MA; [2]RNA Therapeutics Institute, University of Massachusetts Medical School, Worcester, MA; [3]Department of Computer Science, University of Central Florida, Orlando, FL; [4]Kavli Institute for the Physics and Mathematics of the Universe, University of Tokyo, Kashiwa, Japan.

*H. Ma, L.-C. Tu, and Y.-C. Chung contributed equally to this paper; Correspondence to Thoru Pederson: thoru.pederson@umassmed.edu; H. Ma's present address is School of Life Science and Technology, ShanghaiTech University, Shanghai, China; L.-C. Tu and Y.-C. Chung's present address is Department of Biological Chemistry and Pharmacology, Ohio State University, Columbus, OH.

Check for updates

measurements made on populations of cells, has recently been overcome by refinements that enable single cell–based analysis (Nagano et al., 2013, 2017; Stevens et al., 2017).

Little is known about the inter-locus distances and domain dynamics of interphase chromosomes in living cells (Giorgetti and Heard, 2016; Nozaki et al., 2017). Building on our CRISP-Rainbow system (Ma et al., 2016a), we developed a brighter, multicolor CRISPR-based DNA imaging system, "CRISPR-Sirius" (Ma et al., 2018), which enabled resolution of these genomic features from the kilobase to megabase scale in real time. We tracked pairs of loci separated by distances ranging from 4.6 kb to 4.2 Mb and observed two distinct modes of dynamics: relative and centroid movements of the domain.

As described in our recent publication on CRISPR-Sirius (Ma et al., 2018), it is not straightforward to define genomic repeats that are on the one hand restricted to a particular chromosome and, on the other, are present at certain locations at copy numbers ideal for detection by our labeling method. Through our comprehensive bioinformatics mining of all the human repeats (see Materials and methods), we chose a particular locus for the present study that met these criteria. Numerous other such loci that are chromosome-specific and of suitable copy number for labeling have been identified (Fig. S1 in Ma et al., 2018) that can serve as the foundation for expanded future studies.

Results and discussion

Relative and centroid movements of chromosomes revealed by CRISPR-based imaging

CRISPR-Cas9 has been repurposed for tracking chromosomal loci in living cells (Chen et al., 2013), and orthogonal Cas9s with their cognate guide RNAs subsequently were developed to target and visualize multiple loci in single cells (Ma et al., 2015, 2016b; Chen et al., 2016; Gu et al., 2018). Innovative methods based on fluorescent reporters other than dCas9-guide RNAs have also recently been introduced and used to track multiple loci (Kepten et al., 2015; Germier et al., 2017). Here we used a sensitive CRISPR-based DNA imaging method, CRISPR-Sirius (Fig. 1, A and B), for imaging the dynamics of 4.6-kb-spaced IDR2/IDR3 loci (Ma et al., 2018) in human U2OS cells (Fig. 1 C). Both IDR2 and IDR3 are chromosome-specific repeats. IDR2 contains 36 copies of CRISPR target sites in an ~1.0-kb region, while IDR3 contains 45 copies of CRISPR target sites in an ~1.9-kb region (Ma et al., 2018). We observed major differences in the dynamic properties of this locus pair of IDR2 and IDR3 over time in two different cells (Fig. 1, D and E). It can be seen that the range of movements of the site is distinctly greater in cell 2 than cell 1. The trajectory radii for IDR2 (R_{IDR2}) and IDR3 (R_{IDR3}) were 68 nm and 72 nm, respectively, in cell 1 (Fig. 1 D), while they were 153 nm for IDR2 and 180 nm for IDR3 in cell 2 (Fig. 1 E). To further understand the dynamic inter-locus distance change, we invested its diffusive motion by calculating the mean square displacement (MSD), the gyration radius of trajectory (trajectory radius), and relative angle (see Materials and methods, Quantification of distance and movement of locus pairs). The diffusive dynamics can be characterized by the scaling exponent of the

MSD plotted versus the lag time as super-diffusion (exponent > 1), normal diffusion (exponent = 1), or sub-diffusion (0 < exponent < 1; Dion and Gasser, 2013). The diffusive motion of a locus reports information on its local environment. Here we are more concerned about the detection of dynamic inter-locus distance changes during the cell cycle. Therefore, instead of investigating the dynamics of (two) individual loci, we considered it as a two-locus system and decomposed its dynamics into relative and centroid movements. Both movements demonstrated distinct diffusive behavior during the cell cycle. The former is likely correlated with chromatin folding changes, whereas the latter might describe "domain" movement of the system.

To measure the relative movements of this pair of loci, one (IDR3) was used as a spatial reference, and the relative motion of the other (IDR2; $R_{A/B}$ in Fig. 1 F) as well as the relative angles were determined as a function of time (θ_R in Fig. S1, A and B). The relative trajectory radii of the IDR2 and IDR3 pair were 25 nm in cell 1 (Fig. 1 G) and 143 nm in cell 2 (Fig. 1 H), indicating higher relative dynamics of this chromosomal fiber in the latter. To measure the movement of the IDR2/IDR3-spanning genomic region itself, the trajectory radius of the centroid was calculated (Fig. 1 I). As shown in Fig. 1, J and K, the radius of the centroid in cell 1 was 69 nm and 151 nm in cell 2, indicating higher mobility of this domain in the latter. There are no genes between IDR2 and IDR3, and the closest active gene (MIER2) is more than 30 kb from this locus pair (Fig. 1 L). Whether transcriptional activation or silencing in the distal regions affects the dynamics of the locus pair we tracked is yet to be determined. In this study, we focus specifically on how the dynamics of this locus pair are related to the cell cycle.

As can be seen in Fig. 2 A and Table 1, the relative MSDs of the locus pair IDR2/IDR3 are best fitted as sub-diffusion with exponents less than one in the period of measuring time, and fall into three populations. The low population plateaued at ~0.005 μm^2 with a diffusion constant $5.28 \pm 0.32 \times 10^{-4}$ and exponent $1.37 \pm 0.15 \times 10^{-1}$, the middle one reached ~0.015 μm^2 with a diffusion constant $1.55 \pm 0.04 \times 10^{-3}$ and exponent $2.09 \pm 0.07 \times 10^{-1}$, and the high MSD reached ~0.030 μm^2 with a diffusion constant $4.76 \pm 0.21 \times 10^{-3}$ and exponent $1.19 \pm 0.11 \times 10^{-1}$. As shown in Fig. 2 B, the relative trajectory radii increased from the low to high MSD populations. The maximal spatial distance (D_{Max}) represents the contortion of the locus pair or compaction/relaxation of the chromosomal fiber in this kilobases' domain, which also increased from the low to high MSD populations (Fig. S1, C and D). The positive correlation of maximal spatial distance and relative trajectory radii indicated that the compactness of the chromosomal fiber is closely related to its relative mobility.

### Cell cycle–dependent chromosome dynamics in the interphase nucleus

A likely basis for the cell-to-cell variation in the dynamic parameters we have observed in these randomly growing cell populations could be cell cycle stage. To address this, we constructed U2OS-derived stable cell lines expressing both dCas9 and the suitable colored guide RNAs to label IDR2 and IDR3 (see Materials and methods), synchronized the cells (Fig. 2 C), and tracked relative inter-locus and centroid movements at different
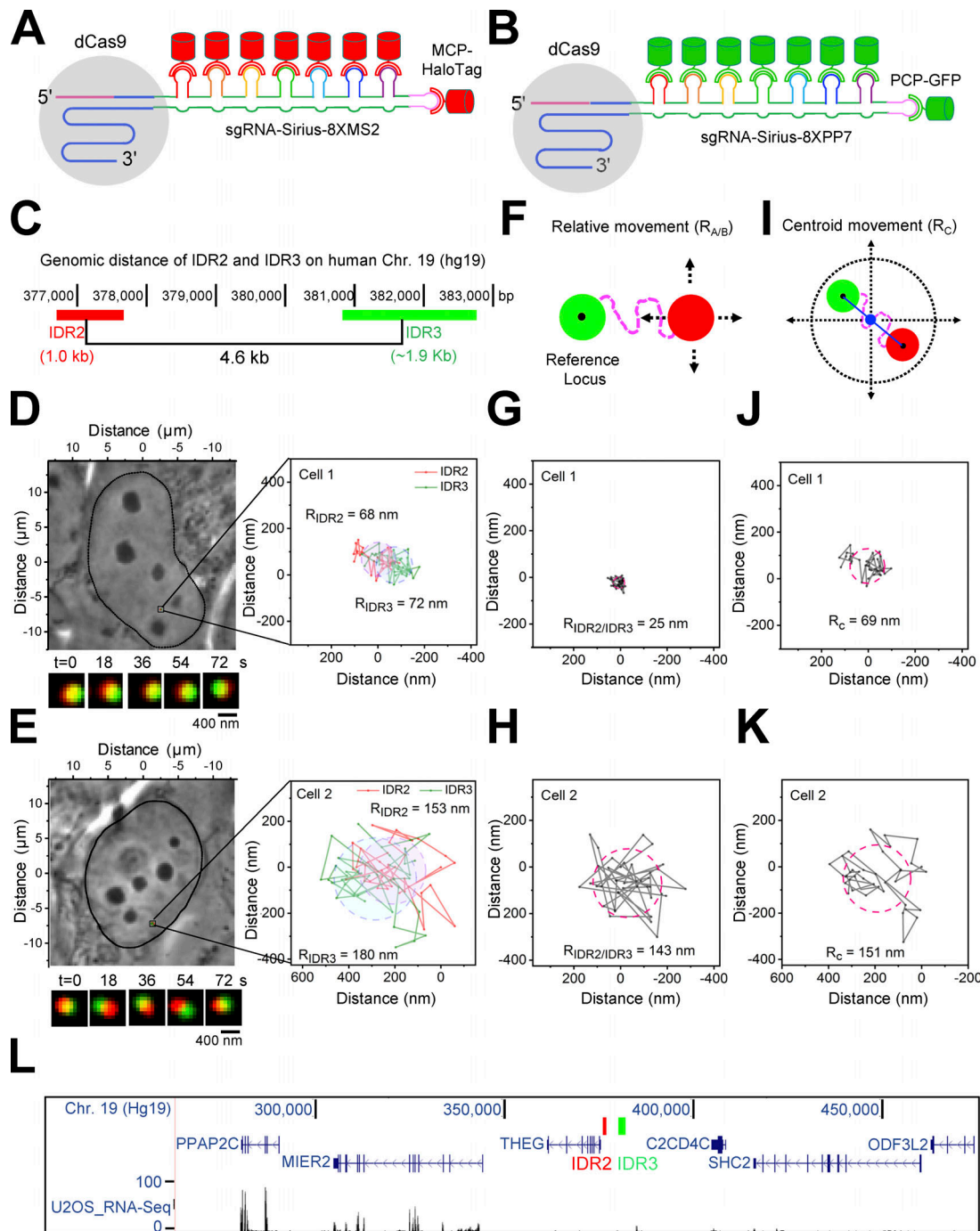
Figure 1. **Relative and centroid dynamics of a locus pair situated at a 4.6-kb distance. (A and B)** Diagram of CRISPR-Sirius design. **(C)** Genomic location of IDR2 and IDR3 with their 4.6-kb inter-locus distance. **(D and E)** Contrasting mobilities of the IDR2/IDR3 locus pair in two cells. Phase contrast images, gyration radius of trajectory (R_{IDR2} and R_{IDR3}), and dual-color time-lapse images were shown in for each cell. **(F)** Schematic of relative movement ($R_{A/B}$) using the IDR3 locus as a reference point. **(G and H)** Relative gyration radii of IDR2 and IDR3 ($R_{IDR2/IDR3}$) in cell 1 and cell 2. **(I)** Diagram of the centroid movement. **(J and K)** Centroid radius of gyration of IDR2 and IDR3 (R_C) in two cells. **(L)** The RNA-Seq of U2OS showed the transcription of genes adjacent to IDR2 and IDR3.

cell cycle stages (Fig. 2, C, and E–H; and Fig. S2, A–D). IDR3/IDR3 was in the range of 30–60 nm with a median of 42 nm, which is significantly less than that of the 4.6 kb–spaced locus pair (Fig. 2 D). As shown in Fig. 2 C, the relative MSD curve of the pair of loci was low, with a diffusion constant $4.10 ± 0.19 × 10^{-4}$ and exponent $2.68 ± 0.15 × 10^{-1}$ in early gap 1 (G1), reaching a maximum with a diffusion constant $4.31 ± 0.08 × 10^{-3}$ and

exponent $1.55 ± 0.06 × 10^{-1}$ in late G1, then decreased in early S with a diffusion constant $3.53 ± 0.07 × 10^{-3}$ and exponent $1.30 ± 0.06 × 10^{-1}$ and then declined to a low level again in mid-late S with a diffusion constant $1.28 ± 0.02 × 10^{-3}$ and exponent $1.07 ± 0.04 × 10^{-1}$. The average relative radii of trajectories between the two loci were calculated (Table 1) and are plotted in Fig. 2 D: $4.04 ± 1.25 × 10^{-2}$ µm in early G1, $1.09 ± 0.26 × 10^{-1}$ µm in late
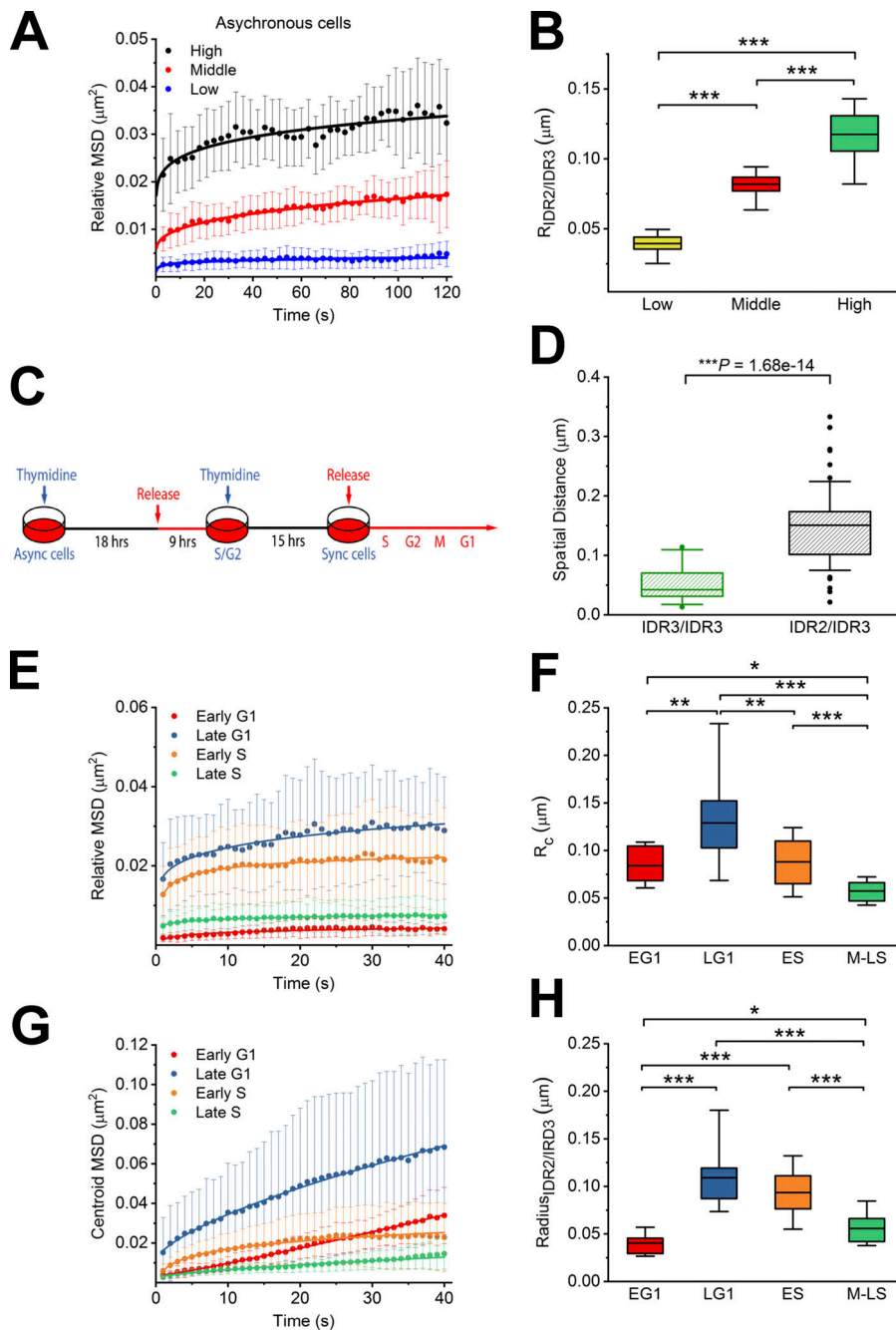
Figure 2. **Distinct chromosome dynamics during cell cycle progression in interphase.** **(A)** Relative MSD of IDR2 and IDR3 pair from asynchronous cells was classified into low, middle, and high MSD groups. n = 13 trajectories for high, n = 11 for middle, and n = 5 for low MSD. The error bars of the MSD plot represent 1 SD. **(B)** Box-and-Whisker plots of relative trajectory radius ($R_{IDR2/IDR3}$) in the low, middle, and high MSD groups. **(C)** Schematic of cell synchronization using double thymidine block. Sync, synchronous; Async, asynchronous. **(D)** Box-and-whisker plots of IDR3/IDR3 (zero genomic distance, n = 24) and IDR2/IDR3 (4.6-kb genomic distance, n = 63). **(E and F)** Relative MSD plot and relative radius ($R_{IDR2/IDR3}$) of IDR2/IDR3 in early G1 (EG1), late G1 (LG1), early S (ES), and mid-late S (M-LS), respectively. n = 5 trajectories for early G1, n = 19 for late G1, n = 21 for early S, and n = 24 for mid-late S. The error bars of the MSD plot represent 1 SD. **(G and H)** Centroid MSD plot and centroid radius of IDR2/IDR3 in early G1, late G1, early S, and mid-late S, respectively. n = 5 trajectories for early G1, n = 19 for late G1, n = 21 for early S, and n = 24 for mid-late S. Significance tests were performed using an unpaired t test: significant difference *, $P < 0.05$; **, $P < 0.01$; ***, $P < 0.001$. The error bars of the MSD plot represent 1 SD.

G1, $9.35 \pm 2.57 \times 10^{-2}$ µm in early S, and $5.57 \pm 1.51 \times 10^{-2}$ µm in mid-late S. Although these MSD curves were best fitted by sub-diffusion, they approximately reached plateaus, especially in the mid-late S and early S. The relative dynamics may be constrained by the environment explored by the locus pairs. The faster reaching plateaus and smaller trajectory radii suggest a more constrained or confined environment, which may be caused by chromatin compaction change during the cell cycle. As shown in Fig. 2 E, the centroid MSD was low in early G1, maximum in late G1, then declining in early S and reaching a minimum in mid-late S. The average centroid radii of trajectory were $8.41 \pm 2.17 \times 10^{-2}$ µm in early G1, $1.29 \pm 0.47 \times 10^{-1}$ µm in late G1, $8.79 \pm 2.64 \times 10^{-2}$ µm in early S, and $5.73 \pm 1.13 \times$ 10^{-2} µm in mid-late S (Table 1 and Fig. 2 F). As shown in Fig. S2 E, the maximal inter-locus distances underwent similar changes, indicating the decompaction of this chromosome region from early G1 to late G1 and then condensation during S phase, which is consistent with results from live cell chromosome accessibility measurements (Pederson and Robbins, 1972). The distribution of relative angles is narrower in early G1 and mid-late S than late G1 and early S (Fig. S2 F), further supporting the changes in chromosome mobility. These results indicate intrinsic constraints such as folding (Nagano et al., 2017) could be the determinant for local dynamics, and external constraints such as the local environment (Ou et al., 2017) might be essential for chromosomal domain dynamics.

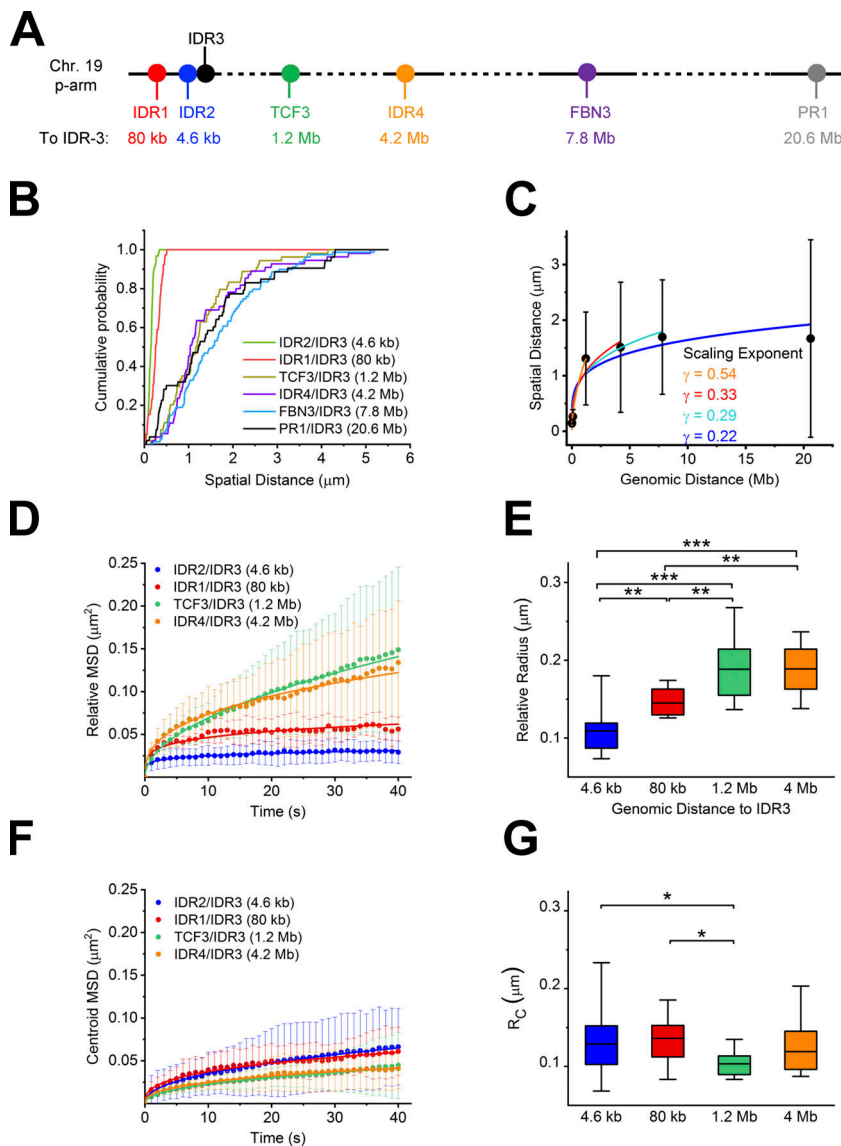Table 1. **Biophysical parameters extracted from loci pair trajectories**

Figure	MSD curve	Diffusion constant D_{diff} ($\mu m^2/s^\alpha$)	Exponent (α)	Radius (μm)	n (trajectory)
Fig. 2 A	High level	4.76×10^{-3}	1.19×10^{-1}	$(1.18 \pm 0.17) \times 10^{-1}$	13
Fig. 2 A	Middle level	1.55×10^{-3}	2.09 ± 10^{-1}	$(8.19 \pm 0.82) \times 10^{-2}$	11
Fig. 2 A	Low level	5.28×10^{-4}	1.37×10^{-1}	$(3.94 \pm 0.94) \times 10^{-2}$	5
Fig. 2 C	EG1_Relative	4.10×10^{-4}	2.68×10^{-1}	$(4.04 \pm 1.25) \times 10^{-2}$	5
Fig. 2 C	LG1_Relative	4.31×10^{-3}	1.55×10^{-1}	$(1.09 \pm 0.26) \times 10^{-1}$	19
Fig. 2 C	ES_Relative	3.53×10^{-3}	1.30×10^{-1}	$(9.35 \pm 2.57) \times 10^{-2}$	21
Fig. 2 C	M-LS_Relative	1.28×10^{-3}	1.07×10^{-1}	$(5.57 \pm 1.51) \times 10^{-2}$	24
Fig. 2 E	EG1_Centroid	4.35×10^{-4}	7.82×10^{-1}	$(8.41 \pm 2.17) \times 10^{-2}$	5
Fig. 2 E	LG1_Centroid	3.17×10^{-3}	4.51×10^{-1}	$(1.29 \pm 0.47) \times 10^{-1}$	19
Fig. 2 E	ES_Centroid	1.77×10^{-3}	3.59×10^{-1}	$(8.79 \pm 2.64) \times 10^{-2}$	21
Fig. 2 E	M-LS_Centroid	6.60×10^{-4}	4.09×10^{-1}	$(5.73 \pm 1.13) \times 10^{-2}$	24
Fig. 3 B	4.6 kb_Relative	4.36×10^{-3}	1.57×10^{-1}	$(1.12 \pm 0.22) \times 10^{-1}$	19
Fig. 3 B	80 kb_Relative	7.19×10^{-3}	2.08×10^{-1}	$(1.57 \pm 0.15) \times 10^{-1}$	7
Fig. 3 B	1.2 Mb_Relative	5.33×10^{-3}	5.12×10^{-1}	$(2.09 \pm 0.51) \times 10^{-1}$	12
Fig. 3 B	4.2 Mb_Relative	7.95×10^{-3}	3.65×10^{-1}	$(2.09 \pm 0.46) \times 10^{-1}$	11
Fig. 3 D	4.6 kb_Centroid	3.17×10^{-3}	4.43×10^{-1}	$(1.44 \pm 0.47) \times 10^{-1}$	19
Fig. 3 D	80 kb_Centroid	4.25×10^{-3}	3.41×10^{-1}	$(1.45 \pm 0.30) \times 10^{-1}$	7
Fig. 3 D	1.2 Mb_Centroid	1.98×10^{-3}	4.52×10^{-1}	$(1.17 \pm 0.26) \times 10^{-1}$	12
Fig. 3 D	4.2 Mb_Centroid	2.64×10^{-3}	3.71×10^{-1}	$(1.19 \pm 0.26) \times 10^{-1}$	11

Genomic distance–dependent dynamics of locus pairs from kilobases to megabases

The interphase chromosomes are folded in 3D with a hierarchy of architectures at different length scales from sub-kilobase to megabases (Risca and Greenleaf, 2015). Less is known of the higher-order structure and dynamics beyond nucleosomes at scales such as few to tens of kilobases (e.g., regulatory elements), hundreds of kilobases (e.g., TADs) from chromosome capture methods (Rao et al., 2014), and megabase chromosomal domains visualized by microscopy (Cremer and Cremer, 2001). Here we quantified the average inter-locus distance of locus pairs from kilobases to megabases including 4.6 kb (IDR2/IDR3), 80 kb (IDR1/IDR3), 1.2 Mb (TCF3/IDR3), 4.2 Mb (IDR4/IDR3), 7.8 Mb (FBN3/IDR3), and 20.6 Mb (PR1/IDR3; Fig. 3 A). As shown in the cumulative probability plots in Fig. 3 B, the observed mean inter-locus distances positively correlated with the genomic distance within 1 Mb and become less different when further increased the genomic distance, suggesting a diversity of chromosome folding states and inter-locus distances at the kilobase to megabase scales. The mean spatial distance between loci when scaled to the genomic distance has been proposed to plot as a power law with the ~0.3 exponent expected from an ideal fractal-globule polymer model (Wang et al., 2016). This exponent for the PR1/IDR3 20 Mb domain of chromosome 19 was measured to be 0.22 (Fig. 3 C), which is nearly identical to the exponent 0.21, estimated in fixed cells by FISH (Wang et al., 2016). The exponents progressively decreased as the inter-locus distance increased while the degree of variation decreased. These results indicate a positive correlation between the measured

inter-locus distances and the known genomic distances within 1 Mb but which deviates when they are further apart.

We then chose four pairs of loci, 4.6 kb (IDR2/IDR3), 80 kb (IDR1/IDR3), 1.2 Mb (TCF3/IDR3), and 4.2 Mb (IDR4/IDR3), to measure their dynamics. We tracked their movements relative to each other and thereby explore how inter-locus distances contribute to the local and domain dynamics of these chromosomal sites. Late G1 phase was chosen for this comparison as substantially relative movement and centroid (domain) movement of the 4.6 kb IDR2/IDR3 pair was observed in this cell cycle stage. The data and analysis show (Table 1) that both dynamics of locus pairs are best fitted by sub-diffusion with exponents less than one in the period of measuring time. As shown in Fig. 3 D, the relative MSD for the 4.6-kb pair (IDR2/IDR3) plateaued at ~0.03 μm^2, and the 80-kb pair (IDR1/IDR3) at ~0.06 μm^2, while the 1.2-Mb pair (TCF3/IDR3) and 4.2-Mb pair (IDR4/IDR3) MSD curves reached ~0.14 μm^2 without plateauing. To further quantify the dynamics, we calculated the trajectory radius as shown in Table 1. The average radii of trajectories increased from $1.12 \pm 0.22 \times 10^{-1}$ μm for the 4.6-kb pair (IDR2/IDR3), or $1.45 \pm 0.18 \times 10^{-1}$ μm for the 80-kb pair (IDR1/IDR3) to $2.09 \pm 0.51 \times 10^{-1}$ μm for the 1.2-Mb pair (TCF3/IDR3), and no further increase for the 4.2-Mb pair (IDR4/IDR3; $2.09 \pm 0.46 \times 10^{-1}$ μm; Fig. 3 E and Table 1). The trajectory radius measures the mobility as a function of time and can also be regarded as the effective confined radius of the dynamics before reaching plateaus (also see length of constraint in Amitai et al., 2017). These results show that the trajectory radii of relative dynamics expand along with the increase of genomic distance within 1 Mb but deviate

Ma et al.
Cell cycle–dependent chromosome dynamics

Journal of Cell Biology
https://doi.org/10.1083/jcb.201807162

1471

Figure 3. **Spatial distance and dynamics of locus pairs situated at kilobase to megabase apart. (A)** Diagram of loci on the p-arm of chromosome 19 with distances from IDR3 of 4.6 kb (IDR2), 80 kb (IDR1), 1.2 Mb (TCF3), 4.2 Mb (IDR4), 7.8 Mb (FBN3), and 20.6 Mb (PR1). **(B)** Cumulative probability plot showing the difference of spatial distances distribution of inter-locus distances of each pair. **(C)** Mean spatial distance versus genomic distance for all loci pairs. The scaling exponents γ are given by fitting the data to the power law relationship, Mean spatial distance ∝ (genomic distance)^γ. The error bars of the plot represent 1 SD. **(D and E)** Relative MSD and relative radius of loci pairs from IDR2/IDR3 (4.6 kb), IDR1/IDR3 (80 kb), TCF3/IDR3 (1.2 Mb), to IDR4/IDR3 (4.2 Mb). n = 19 trajectories for IDR2/IDR3, n = 7 for the IDR1/IDR3 pair, n = 12 for TCF3/IDR3, and n = 11 for IDR4/IDR3. The error bars of the MSD plot represent 1 SD. **(F and G)** Centroid MSD and centroid radius of the indicated locus pairs. n = 19 trajectories for IDR2/IDR3, n = 7 for the IDR1/IDR3 pair, n = 12 for TCF3/IDR3, and n = 11 for IDR4/IDR3. Significance tests were performed using an unpaired t test: significant difference *, $P < 0.05$; **, $P < 0.01$; ***, $P < 0.001$. The error bars of the MSD plot represent 1 SD.

when they are located at megabases apart. Notably, the centroid MSDs of the megabase pairs, the 1.2-Mb pair (TCF3/IDR3), and the 4.2-Mb pair (IDR4/IDR3) are lower than the centroid MSDs of the kilobase pairs. The reduction of centroid motions can be explained by the correlation of the movement of the pair. We calculated the cross-correlation (Ichiye and Karplus, 1991) of four pairs of loci. The mean cross-correlation is 0.67 ± 1.33 for the 4.6-kb pair (IDR2/IDR3), 0.53 ± 0.17 for the 80-kb pair (IDR1/IDR3), 0.10 ± 0.21 for the 1.2-Mb pair (TCF3/IDR3), and 0.21 ± 0.18 for the 4.2-Mb pair (IDR4/IDR3). As expected, the motions of the 1.2-Mb pair (TCF3/IDR3) and 4.2-Mb pair (IDR4/IDR3) are less correlated than others, which is consistent with their lower centroid motions.

The measurements of MSD and trajectory radius for individual loci are presented in Fig. S3 and Table S1. The MSDs of individual loci were demonstrated to be sub-diffusive motions with exponents ranging between 3.41 and 4.60, consistent with previous results (Stanyte et al., 2018). As shown in Fig. S3 A and Table S1, the average size of explored space of individual loci,

measured as the square root of the MSD, ranged from 251 nm to 291 nm during 40 s, comparable with the 220–280 nm values reported in Stanyte et al. (2018) The average trajectory radius of individual loci ranging between 128 nm and 158 nm (Fig. S3 B and Table S1) is consistent with the constraint length ∼150 nm in Chen et al. (2013). When the centroid MSDs and trajectory radii were measured, however, an opposite pattern emerged for their relationship with genomic distance (Fig. 3, F and G). RNA-Seq data showed there are both active or inactive genes adjacent of these loci (Fig. S3, C–E). The question naturally arises as to whether transcriptional activity or inactivity is at play in the dynamics we have measured. In this regard, it is noteworthy that the one locus pair (TCF3/IDR3) that includes a transcriptionally active site displayed one of the largest relative MSDs and relative radii, and one of the lowest centroid MSDs and centroid radii, raising the possibility that transcription is a factor in the observed dynamics of this locus pair.

It is also to be borne in mind that the presence of the dCas9-guide RNA complex at the target site could be sensed by the cell

as a form of DNA damage, either locally due to the R-loop on the DNA target created by the guide RNA, or perhaps nearby, with either of these envisioned scenarios influencing the dynamics of the interrogated locus. We are currently investigating this point both for dCas9-based labeling and nuclease-active Cas9, the latter addressing how the chromosomal dynamics of a local target being targeted for editing might influence the genomic outcome, and/or the systems response of the cell.

The cell cycle axis of the 4D nucleome
Human genomes are organized in a hierarchical manner in the nucleus (Gibcus and Dekker, 2013; Rao et al., 2014). However, little is understood about interphase chromosome dynamics at the kilobase to megabase scales. Here we applied CRISPR-based multicolor imaging technology to uncover the spatial and temporal features of chromosome dynamics. We focused on a 4.6-kb locus pair, which was estimated to include ~20 nucleosomes and span ~600 nm at maximum elongation, based on the beads-on-a-string model (Szerlong and Hansen, 2011). We demonstrated that this chromosomal region's local relaxation and dynamics are cell cycle–dependent with low local mobility at early G1 and mid-late S, and high at late G1 and early S (Fig. 4). Recent single-cell Hi-C data across the cell cycle showed that condensation of intra-TADs regions increased at mid-late S phase (Nagano et al., 2017), which is consistent with our findings of low local chromosomal fiber relaxation and dynamics in mid-late S phase, although direct comparisons of Hi-C data and live cell imaging–tracking studies are presently somewhat challenging.

In considering the underlying basis for the observed cell cycle–dependent changes in dynamics, the possibility of shifts in transcriptional activity is an obvious possibility. However, only one of the pairs of loci that were tracked includes a transcription unit, namely the *TCF3* gene (Fig. S3 D), and yet all of the other locus pairs studied displayed the same cell cycle–dependent changes in dynamics as that one. A second possibility is that the chromosomal region we have tracked undergoes changes in its degree of tethering to other nuclear structures during the cell cycle (e.g., another chromosome, the lamina, nucleolus, etc.). Increased mobility of the studied region might reflect release from a less mobile structure or increased association with a less mobile one, and decreased mobility of the tracked region could reflect either of the converse situations. Exploration of these tethering scenarios would require the deployment of penetrative biophysical methods in future studies. It is also to be borne in mind that the present study examined the dynamics of locus pairs only at one particular region of one of the chromosomes, and contrasting patterns of dynamics may well be occurring elsewhere in the genome.

Materials and methods
Mining chromosome-specific repeats for the human genome
Human reference genome (assembly GRC h37/hg19; https://genome.ucsc.edu) was analyzed to find target regions and design guide RNAs. The bioinformatics tool Tandem Repeat Finder (Benson, 1999) was used to identify tandem repeats with repeats period length smaller or equal to 2,000 bp in the human genome.

The bioinformatics tool Jellyfish (Marçais and Kingsford, 2011) was used to identify tandem repeats with repeat length longer than 2,000 bp in the human genome.

Plasmid construction
The expression vector for dCas9 (nuclease-dead) from *Streptococcus pyogenes* was that originally constructed from pHAGE-TO-DEST (Ma et al., 2016b) into which the heat stable antigen (HSA) was inserted at the C terminus separated by P2A, resulting in pHAGE-TO-dCas9-P2A-HSA. PCP-GFP was previously described (Ma et al., 2016a), and HaloTag was subcloned to replace the GFP in the pHAGE-EFS-MCP-HaloTag plasmid. The expression vector for guide RNAs was based on the pLKO.1 lentiviral expression system, in which PUR-P2A-BFP was inserted right after the PGK promoter, with either single guide RNA (sgRNA)-8XMS2 or sgRNA-8XPP7 inserted immediately after the mouse U6 (mU6) or human U6 (hU6) promoters, resulting in pPUR-P2A-BFP-mU6-sgRNA-Sirius-8XMS2 or pPUR-P2A-BFP-hU6-sgRNA-Sirius-8XPP7, respectively. All the dCas9 and guide RNA expression vectors reported here will be deposited at Addgene.

Cell culture, transfection, and cell cycle synchronization
Human osteosarcoma U2OS cells were cultured on 35-mm glass-bottom dishes (MatTek) at 37°C in DMEM (Life Technologies) containing high glucose and supplemented with 10% (vol/vol) FBS. For transfection, typically 200 ng of dCas9 plasmid DNA and 1 µg of plasmid DNA for desired guide RNAs were cotransfected using Lipofectamine 2000 (Life Technologies), and the cells were incubated for another 24–48 h before imaging. The stable cell line U2OS^IDR2/IDR3 (see Flow cytometry and stable cell selection) was synchronized by double thymidine block based on cell cycle distribution of U2OS (Karanam et al., 2012). Cells were blocked by 2 mM double thymidine for 18 h, released by rinsing in PBS, and then cultured in fresh medium for 9 h, followed by a second exposure to thymidine for 15 h. The cells were then released again and captured images at 0 h (early S), 4 h (mid-late S), 12 h (early G1), and 17 h (late G1), respectively.

Lentivirus production and transduction
HEK293T cells were maintained in Iscove's Modified Dulbecco's Medium (Thermo Fisher Scientific) containing high glucose and supplemented with 1% GlutaMAX (Life Technologies), 10% FBS (Hycolne FBS; Thermo Fisher Scientific) and 1% each penicillin and streptomycin (Life Technologies). 24 h before transfection, ~5 × 10^5 cells were seeded in six-well plates. For each well, 0.5 µg of pCMV-dR8.2 dvpr (Addgene), 0.3 µg of pCMV-VSV-G (Addgene), each constructed to carry HIV long terminal repeats, and 1.5 µg of the plasmid containing the gene of interest were cotransfected by using TransIT transfection reagent (Mirus) according to the manufacturer's instructions. After 48 h, the virus was collected by filtration through a 0.45-µm polyvinylidene fluoride filter (Pall Laboratory). The virus was immediately used or stored at –80°C. For lentiviral transduction, U2OS cells maintained as described above were transduced by Spinfection in six-well plates with lentiviral supernatant for 2 d,
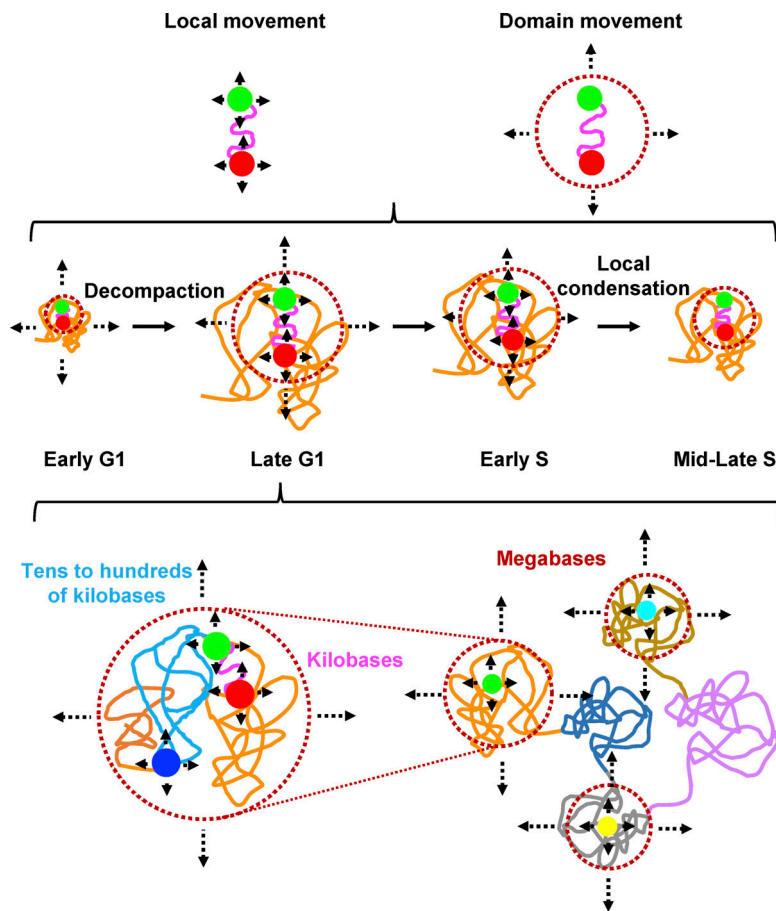
Ma et al.
Cell cycle–dependent chromosome dynamics

Journal of Cell Biology
https://doi.org/10.1083/jcb.201807162

1473

and ∼2 × 10^5 cells were combined with 1 ml lentiviral supernatant and centrifuged for 30 min at 1,200 g.

Flow cytometry and stable cell selection
Cells expressing the desired fluorescent Cas9 and/or guide RNA were selected using a FACSAria cell sorter (BD Bioscience) equipped with 405-, 488-, 561-, and 640-nm excitation lasers, and the emission signals were detected by using filters at 450/50 nm (wavelength/bandwidth) for the Brilliant Violet 421–conjugated anti-mouse CD24 antibody (BioLegend) staining of the HSA, 530/30 nm for PCP-GFP and 582/15 nm for MCP-HaloTag stained with HaloTag-JF549 (Grimm et al., 2015). For the sorting of dCas9 signals, 1 µl of the Brilliant Violet 421–conjugated anti-mouse CD24 antibody was added in a 100-µl cell solution for 30 min before FACS. For sorting of MCP-HaloTag, HaloTag-JF549 was added to the cells at 2 nM 18–24 h before sorting. Single cells were sorted into single wells of 96-well plates containing 1% GlutaMAX, 20% FBS, and 1% penicillin and streptomycin in chilled DMEM. Positive clones of U2OS$^{dCas9-HSA/PCP-GFP/MCP-HaloTag}$ were selected from 96-well plates 10 d later. To generate stable cell lines in which the IDR2/IDR3 locus pair was durably labeled, the U2OS$^{dCas9-HSA/PCP-GFP/MCP-HaloTag}$ cell line was transduced for 48 h by lentivirus for PUR-P2A-BFP-mU6-IDR2-sgRNA-8XMS2-hU6-IDR3-sgRNA-8XPP7-IDR3. Cells were then selected on puromycin for 3–5 d before sorting for BFP, using filters at 405-nm

excitation and 450/50-nm emission. The resulting cell line was simply named U2OS$^{IDR2/IDR3}$.

Fluorescence microscopy
A Leica DMIRB microscope was equipped with an EMCCD camera (Andor iXon-897), mounted with a 2× magnification adapter and 100× oil objective lens (NA 1.4), and resulting in a total 200× magnification equal to a pixel size of 80 nm in the images was used. The microscope stage incubation chamber was maintained at 37°C in Hepes-buffered DMEM with 10% FBS. GFP was excited with an excitation filter at 470/28 nm (Semrock), and its emission was collected using an emission filter at 512/23 nm (Semrock). HaloTag-JF549 was excited at 556/20 nm (Semrock), and its emission was collected in a 630/91 nm channel. Imaging data were acquired by MetaMorph acquisition software (Molecular Devices). Typical tracking was performed with an exposure time of 50 ms for both GFP and HaloTag, and a total of 60 frames of each sample will be collected with either 1-s or 3-s intervals. Most of the data were processed for the first 40 frames due to the signal loss of foci during tracking. The image size was adjusted to show individual nuclei, and intensity thresholds were set on the basis of the ratios between nuclear focal signals to background nucleoplasmic fluorescence. To quantify the spatial distance or track the dynamics, only pairs of loci lying in the same foci plane were analyzed.

Imaging processing of locus pair tracking

The images were analyzed by the Fiji and Mathematica (Wolfram) software. Images from the green and red channels were registered by using a 0.1-μm coverglass-absorbed TetraSpeck fluorescent microsphere (Invitrogen) as a standard sample. In live cell tracking, the specific genomic loci signals were identified and tracked by using the TrackMate plugin (Tinevez et al., 2017). The cell movement was corrected by tracking the centroid of the nucleus over time. Detailed calculation of the MSD, relative spatial distance (D), gyration radius of trajectory radius (R), and relative angle (θ_R) are described in the following section.

Quantification of distance and movement of locus pairs

Let p(t) be the position vector of a locus at time t. The trajectory of the locus is defined by a time series of positions $\{p_0, p_1,...,p_n\}$ where $p_k := p(t_k)$, $t_{k+1} = t_k + \Delta t$, $0 = t_0 < t_1,...,< t_n$, and Δt is a fixed time interval between two successive frames. Given a trajectory $\{p_0, p_1,...,p_n\}$, the associated MSD of lag time $k\Delta t$ is given by

$$MSD(k\Delta t) = \frac{1}{(n-k+1)} \sum_{m=0}^{n-k} |\mathbf{p}(m\Delta t + k\Delta t) - \mathbf{p}(m\Delta t)|^2.$$

Given trajectories $\{p_A(t_0), p_A(t_1),...,p_A(t_n)\}$ and $\{p_B(t_0), p_B(t_1),...,p_B(t_n)\}$ of two loci A and B, the relative and centroid trajectories are defined by $\{p_{A/B}(t_0), p_{A/B}(t_1),...,p_{A/B}(t_n)\}$ and $\{p_C(t_0), p_C(t_1),...,p_C(t_n)\}$, respectively, where $p_{A/B}(t_k) = p_B(t_k) - p_A(t_k)$ with the length

$$D_{A/B}(t_k) = |\mathbf{p}_{A/B}(t_k)| \text{ and } p_C(t_k) = \frac{1}{2}[p_B(t_k) + p_A(t_k)]$$

for k = 0, 1,...,n. Their associated MSDs are denoted by $MSD_{A/B}$ and MSD_C, respectively. All MSD curves were fitted by the power law equation, $MSD(t) = 4D_{diff} t^\alpha$, where D_{diff} is the diffusion constant. All MSDs possessed exponents $0 < \alpha < 1$. In addition to the plots in the figures, all the values are listed in Table 1.

We also defined a time series of the relative angle $\{\theta_R(t_1), \theta_R(t_2),..., \theta_R(t_n)\}$ for the relative trajectory where $\theta_R(t_m)$ is defined by the angle swept from the vector $p_{A/B}(t_{m-1})$ to the vector $p_{A/B}(t_m)$ for m = 1, 2,...,n. The angle was calculated by

$$\theta_R(t_m) = \cos^{-1}\left[\frac{\mathbf{p}_{A/B}(t_{m-1}) \cdot \mathbf{p}_{A/B}(t_m)}{|\mathbf{p}_{A/B}(t_{m-1})||\mathbf{p}_{A/B}(t_m)|}\right],$$

where $-180° \leq \theta_R(t_m) \leq 180°$ with the sign reflecting the orientation of the angle, positive for counterclockwise and negative for clockwise.

In addition to MSD, we also introduce a quantity, named the trajectory radius, to measure the mobility of a locus or locus pair. This trajectory radius is defined as the gyration radius of the points collected from all steps on a trajectory and used to measure the range of the area covered by the trajectory. More precisely, given trajectory $\{p_S(t_0), p_S(t_1),...,p_S(t_n)\}$, S = A, B, A/B, C, the trajectory radius R_S of trajectory S is defined by

$$R_S = \sqrt{\frac{1}{(n+1)} \sum_{k=0}^{n} |\mathbf{p}_S(t_k) - \mathbf{p}_{CT}|^2},$$

where

$$p_{CT} = \frac{1}{(n+1)} \sum_{k=0}^{n} \mathbf{p}_S(t_k)$$

is the geometric center of the positions $\{p_S(t_0), p_S(t_1),...,p_S(t_n)\}$.

γ denotes the scaling exponent of the power law relationship, mean spatial distance $\propto$ (genomic distance)$^\gamma$ and is determined by fitting the power law relationship with experimental data.

All these analyses, including the cumulative probability of loci pairs' spatial distance, were performed by Mathematica, and graphs were generated by OriginPro (OriginLab). All box plots were generated using the default setting of the OriginPro. Box spans from first to last quartiles and whisker length are determined by the outermost data point that falls within the upper inner and lower inner fence (a coefficient = 1.5), except the middle line represents the mean value. Significance tests were performed using an unpaired *t* test and simulated by OriginPro: significant difference *, $P < 0.05$; **, $P < 0.01$; and ***, $P < 0.001$.

The SD for the MSD plots was determined from the graphing program OriginPro (OriginLab) fitting routine.

Analysis of expressed transcripts using RNA-Seq data

The raw reads of the RNA-Seq experiment for the osteosarcoma (U2OS) cell line (Ibarra et al., 2016) were downloaded (GEO accession no. GSM2341646, Run SRR4413995). The raw reads were aligned to the human genome by using bioinformatics tool STAR (Dobin et al., 2013). The generated Binary Alignment Map (BAM) file was sorted by reference coordinates using the bioinformatics tool SAMtools (Li et al., 2009). SAMtools was consequently used to index the BAM file. Bioinformatics tool bamCoverage (Ramírez et al., 2016) was applied to generate the bigWig file from the sorted BAM file and its index. The UCSC Genome Browser was used to visualize the RNA-Seq results using the generated bigWig file.

Online supplemental material

Fig. S1 shows relative angles of IDR2 and IDR3 from two cells and maximal inter-locus distances from distinct MSD groups of IDR2/IDR3. Fig. S2 shows relative and centroid dynamics, maximal inter-locus distance, and relative angles in each cell cycle stage. Fig. S3 shows dynamics of individual loci. Table S1 shows biophysical parameters extracted from individual loci trajectories.

References

Amitai, A., A. Seeber, S.M. Gasser, and D. Holcman. 2017. Visualization of chromatin decompaction and break site extrusion as predicted by statistical polymer modeling of single-locus trajectories. *Cell Reports.* 18:1200–1214. https://doi.org/10.1016/j.celrep.2017.01.018

Benson, G. 1999. Tandem repeats finder: a program to analyze DNA sequences. *Nucleic Acids Res.* 27:573–580. https://doi.org/10.1093/nar/27.2.573

Boettiger, A.N., B. Bintu, J.R. Moffitt, S. Wang, B.J. Beliveau, G. Fudenberg, M. Imakaev, L.A. Mirny, C.T. Wu, and X. Zhuang. 2016. Super-resolution imaging reveals distinct chromatin folding for different epigenetic states. *Nature.* 529:418–422. https://doi.org/10.1038/nature16496

Chen, B., L.A. Gilbert, B.A. Cimini, J. Schnitzbauer, W. Zhang, G.W. Li, J. Park, E.H. Blackburn, J.S. Weissman, L.S. Qi, and B. Huang. 2013. Dynamic imaging of genomic loci in living human cells by an optimized CRISPR/Cas system. *Cell.* 155:1479–1491. https://doi.org/10.1016/j.cell.2013.12.001

Chen, B., J. Hu, R. Almeida, H. Liu, S. Balakrishnan, C. Covill-Cooke, W.A. Lim, and B. Huang. 2016. Expanding the CRISPR imaging toolset with Staphylococcus aureus Cas9 for simultaneous imaging of multiple genomic loci. *Nucleic Acids Res.* 44:e75. https://doi.org/10.1093/nar/gkv1533

Cremer, T., and C. Cremer. 2001. Chromosome territories, nuclear architecture and gene regulation in mammalian cells. *Nat. Rev. Genet.* 2:292–301. https://doi.org/10.1038/35066075

Dion, V., and S.M. Gasser. 2013. Chromatin movement in the maintenance of genome stability. *Cell.* 152:1355–1364. https://doi.org/10.1016/j.cell.2013.02.010

Dobin, A., C.A. Davis, F. Schlesinger, J. Drenkow, C. Zaleski, S. Jha, P. Batut, M. Chaisson, and T.R. Gingeras. 2013. STAR: ultrafast universal RNA-seq aligner. *Bioinformatics.* 29:15–21. https://doi.org/10.1093/bioinformatics/bts635

Flemming, W. 1882. *Zellsubstanz.* Kern und Zelltheilung, Leipzig, Germany. 424 pp.

Francis, N.J., R.E. Kingston, and C.L. Woodcock. 2004. Chromatin compaction by a polycomb group protein complex. *Science.* 306:1574–1577. https://doi.org/10.1126/science.1100576

Germier, T., S. Kocanova, N. Walther, A. Bancaud, H.A. Shaban, H. Sellou, A.Z. Politi, J. Ellenberg, F. Gallardo, and K. Bystricky. 2017. Real-time imaging of a single gene reveals transcription-initiated local

confinement. *Biophys. J.* 113:1383–1394. https://doi.org/10.1016/j.bpj.2017.08.014

Gibcus, J.H., and J. Dekker. 2013. The hierarchy of the 3D genome. *Mol. Cell.* 49:773–782. https://doi.org/10.1016/j.molcel.2013.02.011

Giorgetti, L., and E. Heard. 2016. Closing the loop: 3C versus DNA FISH. *Genome Biol.* 17:215. https://doi.org/10.1186/s13059-016-1081-2

Grimm, J.B., B.P. English, J. Chen, J.P. Slaughter, Z. Zhang, A. Revyakin, R. Patel, J.J. Macklin, D. Normanno, R.H. Singer, T. Lionnet, and L.D. Lavis. 2015. A general method to improve fluorophores for live-cell and single-molecule microscopy. *Nat Methods.* 12:244–250.

Gu, B., T. Swigut, A. Spencley, M.R. Bauer, M. Chung, T. Meyer, and J. Wysocka. 2018. Transcription-coupled changes in nuclear mobility of mammalian cis-regulatory elements. *Science.* 359:1050–1055. https://doi.org/10.1126/science.aao3136

Heun, P., T. Laroche, K. Shimada, P. Furrer, and S.M. Gasser. 2001. Chromosome dynamics in the yeast interphase nucleus. *Science.* 294:2181–2186. https://doi.org/10.1126/science.1065366

Ibarra, A., C. Benner, S. Tyagi, J. Cool, and M.W. Hetzer. 2016. Nucleoporin-mediated regulation of cell identity genes. *Genes Dev.* 30:2253–2258. https://doi.org/10.1101/gad.287417.116

Ichiye, T., and M. Karplus. 1991. Collective motions in proteins: a covariance analysis of atomic fluctuations in molecular dynamics and normal mode simulations. *Proteins.* 11:205–217. https://doi.org/10.1002/prot.340110305

Jubb, A.W., S. Boyle, D.A. Hume, and W.A. Bickmore. 2017. Glucocorticoid receptor binding induces rapid and prolonged large-scale chromatin decompaction at multiple target loci. *Cell Reports.* 21:3022–3031. https://doi.org/10.1016/j.celrep.2017.11.053

Karanam, K., R. Kafri, A. Loewer, and G. Lahav. 2012. Quantitative live cell imaging reveals a gradual shift between DNA repair mechanisms and a maximal use of HR in mid S phase. *Mol. Cell.* 47:320–329. https://doi.org/10.1016/j.molcel.2012.05.052

Kepten, E., A. Weron, I. Bronstein, K. Burnecki, and Y. Garini. 2015. Uniform contraction-expansion description of relative centromere and telomere motion. *Biophys. J.* 109:1454–1462. https://doi.org/10.1016/j.bpj.2015.07.031

Li, H., B. Handsaker, A. Wysoker, T. Fennell, J. Ruan, N. Homer, G. Marth, G. Abecasis, and R. Durbin. 1000 Genome Project Data Processing Subgroup. 2009. The sequence alignment/map format and SAMtools. *Bioinformatics.* 25:2078–2079. https://doi.org/10.1093/bioinformatics/btp352

Lieberman-Aiden, E., N.L. van Berkum, L. Williams, M. Imakaev, T. Ragoczy, A. Telling, I. Amit, B.R. Lajoie, P.J. Sabo, M.O. Dorschner, et al. 2009. Comprehensive mapping of long-range interactions reveals folding principles of the human genome. *Science.* 326:289–293. https://doi.org/10.1126/science.1181369

Ma, H., A. Naseri, P. Reyes-Gutierrez, S.A. Wolfe, S. Zhang, and T. Pederson. 2015. Multicolor CRISPR labeling of chromosomal loci in human cells. *Proc. Natl. Acad. Sci. USA.* 112:3002–3007. https://doi.org/10.1073/pnas.1420024112

Ma, H., L.C. Tu, A. Naseri, M. Huisman, S. Zhang, D. Grunwald, and T. Pederson. 2016a. CRISPR-Cas9 nuclear dynamics and target recognition in living cells. *J. Cell Biol.* 214:529–537. https://doi.org/10.1083/jcb.201604115

Ma, H., L.C. Tu, A. Naseri, M. Huisman, S. Zhang, D. Grunwald, and T. Pederson. 2016b. Multiplexed labeling of genomic loci with dCas9 and engineered sgRNAs using CRISPRainbow. *Nat. Biotechnol.* 34:528–530. https://doi.org/10.1038/nbt.3526

Ma, H., L.C. Tu, A. Naseri, Y.C. Chung, D. Grunwald, S. Zhang, and T. Pederson. 2018. CRISPR-Sirius: RNA scaffolds for signal amplification in genome imaging. *Nat. Methods.* 15:928–931. https://doi.org/10.1038/s41592-018-0174-0

Marçais, G., and C. Kingsford. 2011. A fast, lock-free approach for efficient parallel counting of occurrences of k-mers. *Bioinformatics.* 27:764–770. https://doi.org/10.1093/bioinformatics/btr011

Nagano, T., Y. Lubling, T.J. Stevens, S. Schoenfelder, E. Yaffe, W. Dean, E.D. Laue, A. Tanay, and P. Fraser. 2013. Single-cell Hi-C reveals cell-to-cell variability in chromosome structure. *Nature.* 502:59–64. https://doi.org/10.1038/nature12593

Nagano, T., Y. Lubling, C. Várnai, C. Dudley, W. Leung, Y. Baran, N. Mendelson Cohen, S. Wingett, P. Fraser, and A. Tanay. 2017. Cell-cycle dynamics of chromosomal organization at single-cell resolution. *Nature.* 547:61–67. https://doi.org/10.1038/nature23001

Nozaki, T., R. Imai, M. Tanbo, R. Nagashima, S. Tamura, T. Tani, Y. Joti, M. Tomita, K. Hibino, M.T. Kanemaki, et al. 2017. Dynamic organization of

chromatin domains revealed by super-resolution live-cell imaging. *Mol. Cell.* 67:282–293.e7.

Ou, H.D., S. Phan, T.J. Deerinck, A. Thor, M.H. Ellisman, and C.C. O'Shea. 2017. ChromEMT: Visualizing 3D chromatin structure and compaction in interphase and mitotic cells. *Science.* 357:eaag0025. https://doi.org/10.1126/science.aag0025

Pederson, T. 1972. Chromatin structure and the cell cycle. *Proc. Natl. Acad. Sci. USA.* 69:2224–2228. https://doi.org/10.1073/pnas.69.8.2224

Pederson, T., and E. Robbins. 1972. Chromatin structure and the cell division cycle. Actinomycin binding in synchronized HeLa cells. *J. Cell Biol.* 55: 322–327. https://doi.org/10.1083/jcb.55.2.322

Ramírez, F., D.P. Ryan, B. Grüning, V. Bhardwaj, F. Kilpert, A.S. Richter, S. Heyne, F. Dündar, and T. Manke. 2016. deepTools2: a next generation web server for deep-sequencing data analysis. *Nucleic Acids Res.* 44(W1): W160-5. https://doi.org/10.1093/nar/gkw257

Rao, S.S., M.H. Huntley, N.C. Durand, E.K. Stamenova, I.D. Bochkov, J.T. Robinson, A.L. Sanborn, I. Machol, A.D. Omer, E.S. Lander, and E.L. Aiden. 2014. A 3D map of the human genome at kilobase resolution reveals principles of chromatin looping. *Cell.* 159:1665–1680. https://doi.org/10.1016/j.cell.2014.11.021

Risca, V.I., and W.J. Greenleaf. 2015. Unraveling the 3D genome: genomics tools for multiscale exploration. *Trends Genet.* 31:357–372. https://doi.org/10.1016/j.tig.2015.03.010

Robinett, C.C., A. Straight, G. Li, C. Willhelm, G. Sudlow, A. Murray, and A.S. Belmont. 1996. In vivo localization of DNA sequences and visualization of large-scale chromatin organization using lac operator/repressor recognition. *J. Cell Biol.* 135:1685–1700. https://doi.org/10.1083/jcb.135.6.1685

Stanyte, R., J. Nuebler, C. Blaukopf, R. Hoefler, R. Stocsits, J.M. Peters, and D. W. Gerlich. 2018. Dynamics of sister chromatid resolution during cell cycle progression. *J. Cell Biol.* 217:1985–2004. https://doi.org/10.1083/jcb.201801157

Stevens, T.J., D. Lando, S. Basu, L.P. Atkinson, Y. Cao, S.F. Lee, M. Leeb, K.J. Wohlfahrt, W. Boucher, A. O'Shaughnessy-Kirwan, et al. 2017. 3D structures of individual mammalian genomes studied by single-cell Hi-C. *Nature.* 544:59–64. https://doi.org/10.1038/nature21429

Szerlong, H.J., and J.C. Hansen. 2011. Nucleosome distribution and linker DNA: connecting nuclear function to dynamic chromatin structure. *Biochem. Cell Biol.* 89:24–34. https://doi.org/10.1139/O10-139

Teller, K., D. Illner, S. Thamm, C.S. Casas-Delucchi, R. Versteeg, M. Indemans, T. Cremer, and M. Cremer. 2011. A top-down analysis of Xa- and Xi-territories reveals differences of higher order structure at ≥ 20 Mb genomic length scales. *Nucleus.* 2:465–477. https://doi.org/10.4161/nucl.2.5.17862

Tinevez, J.Y., N. Perry, J. Schindelin, G.M. Hoopes, G.D. Reynolds, E. Laplantine, S.Y. Bednarek, S.L. Shorte, and K.W. Eliceiri. 2017. TrackMate: An open and extensible platform for single-particle tracking. *Methods.* 115:80–90. https://doi.org/10.1016/j.ymeth.2016.09.016

Wang, S., J.H. Su, B.J. Beliveau, B. Bintu, J.R. Moffitt, C.T. Wu, and X. Zhuang. 2016. Spatial organization of chromatin domains and compartments in single chromosomes. *Science.* 353:598–602. https://doi.org/10.1126/science.aaf8084